Article

Engineering vacancy and hydrophobicity of two-dimensional $TaTe_2$ for efficient and stable electrocatalytic N_2 reduction

Zhenqing Zhao,[1] Jongseo Park,[2] Changhyeok Choi,[2] Song Hong,[1] Xiangchao Hui,[1] Hao Zhang,[3] Tsz Woon Benedict Lo,[3] Alex W. Robertson,[4] Zengxiang Lv,[1] Yousung Jung,[2,*] and Zhenyu Sun[1,*]

*Correspondence: sunzy@mail.buct.edu.cn (Z.S.); ysjn@kaist.ac.kr (Y.J.)

Received: April 8, 2021; Accepted: November 23, 2021; Published Online: November 27, 2021; https://doi.org/10.1016/j.xinn.2021.100190

GRAPHICAL ABSTRACT

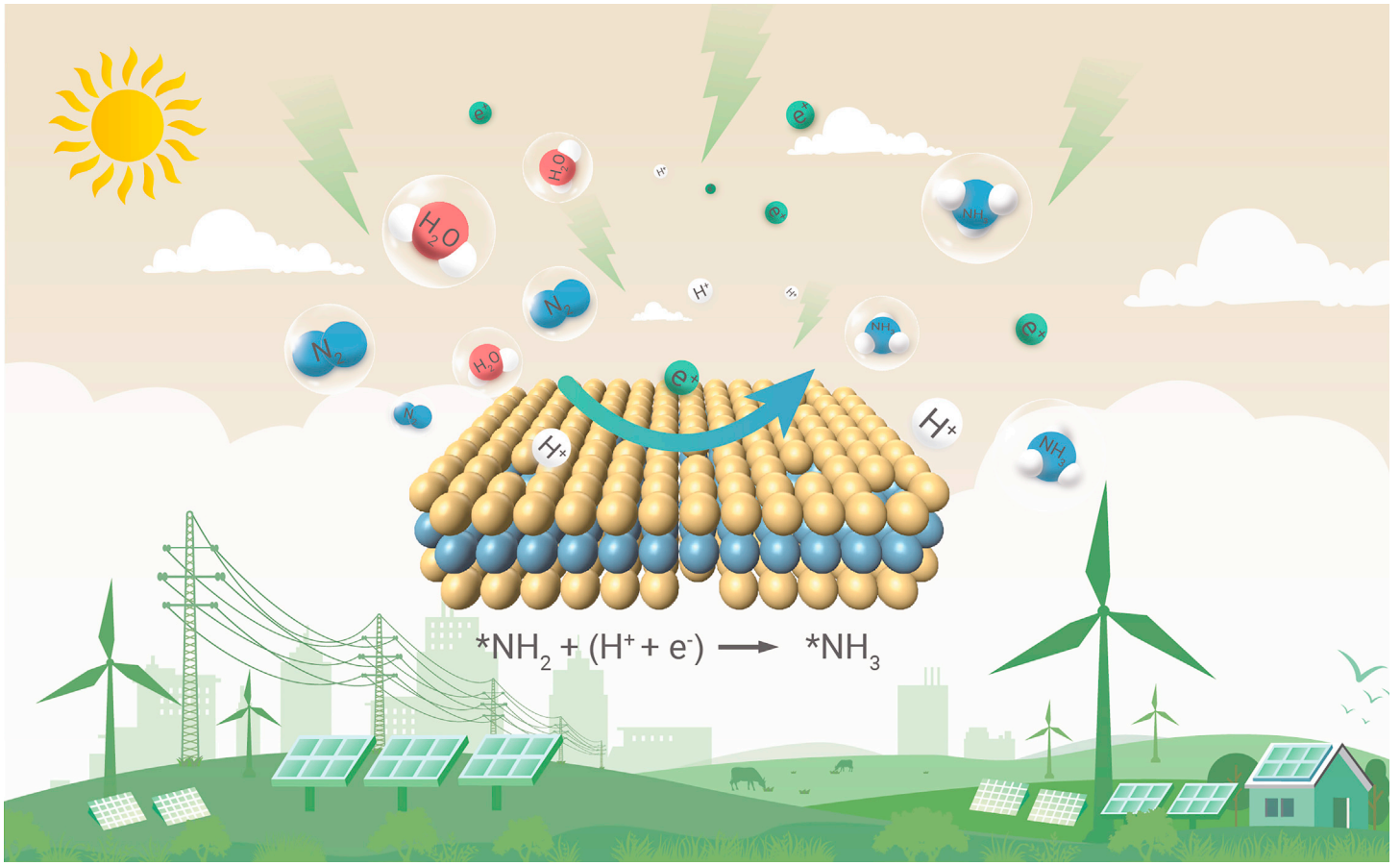

PUBLIC SUMMARY

- 2D $TaTe_2$ is produced in large quantities
- Jointly tuning the Te vacancies (V_{Te}) and surface hydrophobicity of 2D $TaTe_2$ enables efficient and stable electrocatalytic NRR with remarkable NH_3 faradic efficiency
- The edge plane of $TaTe_2$ and V_{Te} serve as the main active sites for NRR
- The free energy change at the potential-determining step on V_{Te}-$TaTe_2$ is comparable with the values at the top of the NRR volcano plots on various transition metal surfaces

Article

Engineering vacancy and hydrophobicity of two-dimensional $TaTe_2$ for efficient and stable electrocatalytic N_2 reduction

Zhenqing Zhao,[1] Jongseo Park,[2] Changhyeok Choi,[2] Song Hong,[1] Xiangchao Hui,[1] Hao Zhang,[3] Tsz Woon Benedict Lo,[3] Alex W. Robertson,[4] Zengxiang Lv,[1] Yousung Jung,[2,*] and Zhenyu Sun[1,*]

[1]State Key Laboratory of Organic–Inorganic Composites, Beijing University of Chemical Technology, Beijing 100029, China

[2]Department of Chemical and Biomolecular Engineering (BK21 four), Korea Advanced Institute of Science and Technology (KAIST), Daejeon 34141, Republic of Korea

[3]Department of Applied Biology and Chemical Technology, The Hong Kong Polytechnic University, Hong Kong, China

[4]Department of Materials, University of Oxford, Oxford OX1 3PH, UK

*Correspondence: sunzy@mail.buct.edu.cn (Z.S.); ysjn@kaist.ac.kr (Y.J.)

Received: April 8, 2021; Accepted: November 23, 2021; Published Online: November 27, 2021; https://doi.org/10.1016/j.xinn.2021.100190

Citation: Zhao Z., Park J., Choi C., et al., (2022). Engineering vacancy and hydrophobicity of two-dimensional $TaTe_2$ for efficient and stable electrocatalytic N_2 reduction. The Innovation **3(1)**, 100190.

Demand for ammonia continues to increase to sustain the growing global population. The direct electrochemical N_2 reduction reaction (NRR) powered by renewable electricity offers a promising carbon-neutral and sustainable strategy for manufacturing NH_3, yet achieving this remains a grand challenge. Here, we report a synergistic strategy to promote ambient NRR for ammonia production by tuning the Te vacancies (V_{Te}) and surface hydrophobicity of two-dimensional $TaTe_2$ nanosheets. Remarkable NH_3 faradic efficiency of up to 32.2% is attained at a mild overpotential, which is largely maintained even after 100 h of consecutive electrolysis. Isotopic labeling validates that the N atoms of formed NH_4^+ originate from N_2. *In situ* X-ray diffraction indicates preservation of the crystalline structure of $TaTe_2$ during NRR. Further density functional theory calculations reveal that the potential-determining step (PDS) is $*NH_2 + (H^+ + e^-) \rightarrow NH_3$ on V_{Te}-$TaTe_2$ compared with that of $* + N_2 + (H^+ + e^-) \rightarrow *N–NH$ on $TaTe_2$. We identify that the edge plane of $TaTe_2$ and V_{Te} serve as the main active sites for NRR. The free energy change at PDS on V_{Te}-$TaTe_2$ is comparable with the values at the top of the NRR volcano plots on various transition metal surfaces.

INTRODUCTION

Nitrogen fixation is a key chemical transformation for sustainable development as ammonia (NH_3) is essential across modern industry and agriculture.[1–4] The traditional fossil-fuel-powered Haber-Bosch process remains widely employed for artificial NH_3 synthesis. However, intense energy consumption (extreme reaction conditions of 300 °C–500 °C and 15–25 MPa),[5] and massive emission of CO_2 (from the reformation of fossil fuels to produce the hydrogen gas feedstock) pose severe technological, environmental, and ecological challenges.[6–10] The electrocatalytic N_2 reduction reaction (NRR), using intermittent electricity generated from renewable sources and water as the hydrogen source, is an attractive strategy for sustainable NH_3 production, and has recently sparked tremendous research interest.[11] However, the cleavage of the inert N_2 molecule is difficult due to its strong dissociation energy (9.756 eV, i.e., ~941 kJ mol^{-1}), high first ionization energy (1,503 kJ mol^{-1}), and short N≡N triple bond (1.098 Å).[12–16] Another issue is that the major competitive reaction, the hydrogen evolution reaction (HER), has faster reaction kinetics and occurs under similar or even lower overpotentials during the NRR with aqueous electrolytes, causing severe energy efficiency losses.[17] Therefore, the design and development of efficient electrocatalysts to break the N≡N bond to drive N_2 conversion while simultaneously suppressing HER is extremely desirable.[18,19] Despite recent efforts, most catalytic systems reported suffer from low selectivity for NH_3 formation (typically less than 15% owing to the concomitant HER), large overpotential (or low energetic efficiency), and insufficient stability (usually <30 h), limiting practical use and technological commercialization.

Transition metal dichalcogenides (TMDs) are an emerging class of two-dimensional (2D) materials possessing direct and tunable band gaps.[20–22] The interatomic binding in TMDs is strong due to covalent in-plane bonding. Nevertheless, the successive layers in TMD materials are bound through weaker van der Waals interlayer forces, which renders these layered materials to be easily exfoliated mechanically.[23] Especially in transition metal tellurides, the relatively low electronegativity of tellurium frequently leads to complex scenarios of competition between metals and non-metals for the bonding electrons. Compared with O, S, and Se chalcogenides, Te has more metallic character, which is a highly desired property for electrocatalysts.[24–26] 2D $TaTe_2$ has been produced by chemical vapor deposition (CVD); however, the route has drawbacks, such as low yield and complicated operation steps, among others. Large-scale synthesis of 2D $TaTe_2$ remains a challenge. Furthermore, the catalytic properties of 2D $TaTe_2$ for NRR are unexplored to date.

Herein, we report efficient production of ultrathin metallic $TaTe_2$ nanosheets with tuned Te vacancies simply via liquid exfoliation of bulk $TaTe_2$. γ-Butyrolactone (γ-BL) was discovered to be an excellent organic solvent for the exfoliation. The specific surface area is maximized for a 2D structure, which affords a potentially high density of active sites and also increases surface accessibility to reactants. In addition, the in-plane electrical conductivity of $TaTe_2$ increased after exfoliation. This provides benefits in electrochemical reactions, where the higher conductivity usually ensures more efficient utilization of the electrical energy. Importantly, the as-prepared defective 2D $TaTe_2$ was found to be active for NRR, affording a remarkable NH_3 faradic efficiency (FE) in excess of 12% and an NH_3 yield rate of about 6.3 μg_{NH3} h^{-1} mg_{cat}^{-1} at a low applied potential of −0.12 V versus the reversible hydrogen electrode (versus RHE). More interestingly, further surface modification of $TaTe_2$ nanosheet electrodes by tethering with trimethoxy (1H,1H,2H,2H heptadecafluorodecyl) silane (TMHFS) could limit the proton transfer on the electrode surface without interrupting the flow of non-polar moieties, thus enhancing the availability of N_2 on the electrode surface in relation to that of the protons. After such hydrophobic treatment of $TaTe_2$ nanosheets (denoted as 2D H-$TaTe_2$), the FE of NH_3 was markedly improved, approaching 32.2%, over 15.4 times compared with bulk $TaTe_2$. The 2D H-$TaTe_2$ catalytic performance was maintained even after 100 h of NRR electrolysis.

RESULTS AND DISCUSSION

Synthesis and structural characterization

We successfully prepared $TaTe_2$ nanosheets by liquid exfoliation of bulk $TaTe_2$ (Figures 1A and 1B) under ultrasound followed by centrifugation (CF) to remove poorly exfoliated aggregates. We discovered seven organic solvents that can effectively delaminate and disperse $TaTe_2$ (Table S1, Figure 1C), namely dimethyl sulfoxide, *N*-methylformamide, 1,3-dimethyl-2-imidazolidinone, γ-BL, tetrahydrofuran, cyclohexanone, and *N*-methyl-2-pyrrolidinone. γ-BL exhibited superior exfoliating capability. The mass of the $TaTe_2$ material after removal of the solvent for specific volumes of dispersions allowed one to estimate the stock dispersion concentration. A sample of the stock dispersion in γ-BL was serially diluted. The absorbance per unit-cell length for each diluted sample was then measured and plotted versus $TaTe_2$ dispersion concentration (Figure S1). The absorption coefficient (α) at 400 nm was derived to be 554.9 mL mg^{-1} m^{-1} by a straight line fit through the points. The resulting concentration (C) after CF was determined according to the Lambert-Beer law ($A = \alpha Cl$, where l is the cell length). The dispersion concentration increased steadily with the initial $TaTe_2$ concentration and reached as high as 4.5 mg mL^{-1} (Figure S2). Analogous to many other 2D materials,[27,28] the dispersion concentration scaled inversely with CF speed (Figure S3). Of interest is that about 80% of the $TaTe_2$ nanosheets maintained a stable dispersion against sedimentation for at least 20 days (Figure S4).

Figure 1D shows powder X-ray diffraction (XRD) patterns of the starting $TaTe_2$ and as-obtained $TaTe_2$ nanosheets. The diffraction peaks at ~13.2°, 30.6°, 31.2°, and 38.8° in traces A and B can be well indexed to the respective (001), (−603), (310), and (−313) reflections of $TaTe_2$ (JCPDS no. 71-2197). This shows that the $TaTe_2$ lattice was preserved after exfoliation. However, dramatic weakening in the

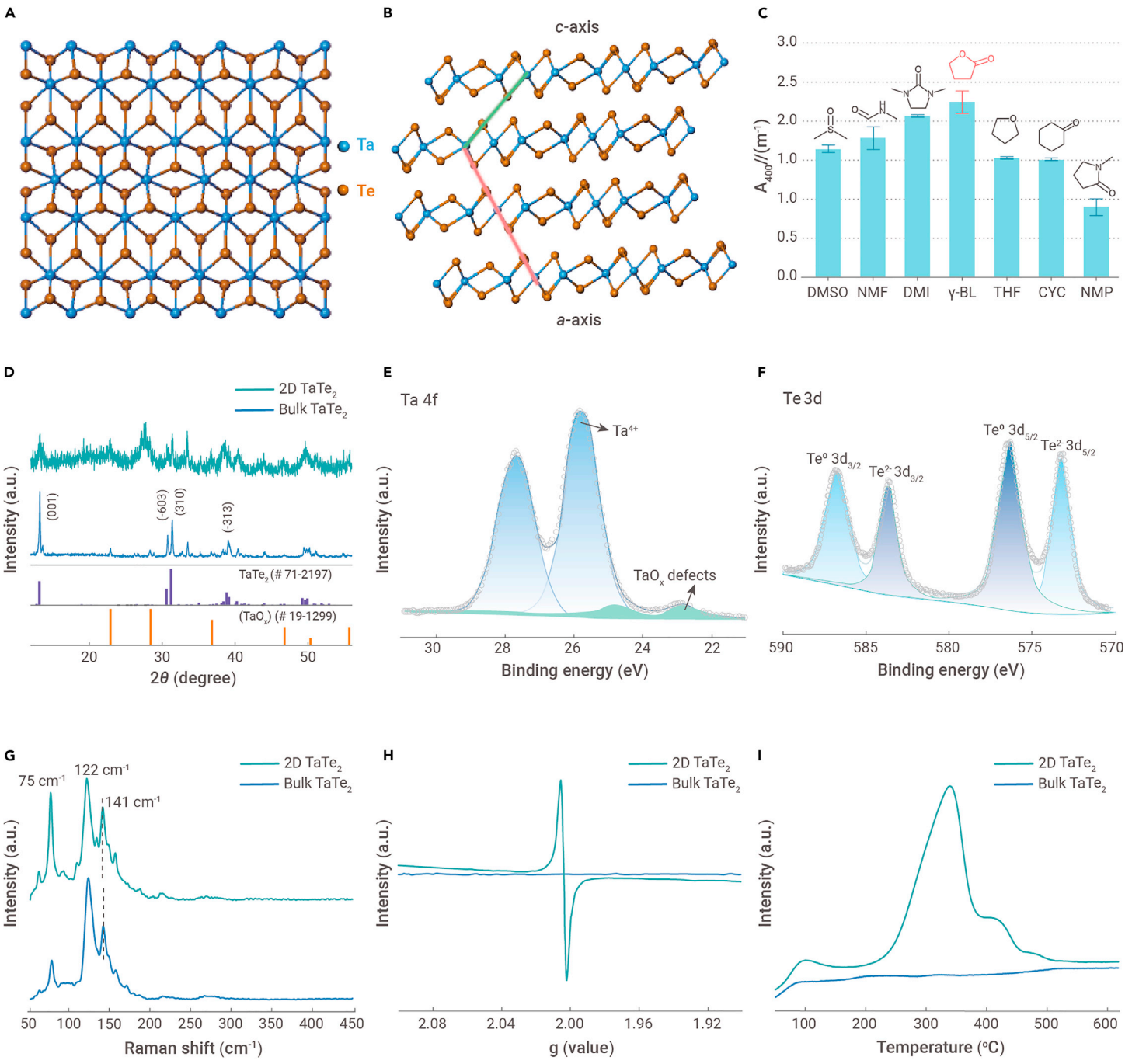

Figure 1. Structure, Surface Composition, and N_2 Adsorption Property of $TaTe_2$ (A and B) (A) Top view and (B) side view of the $TaTe_2$ crystal structure. (C) The absorbance (at 400 nm) per unit-cell length of $TaTe_2$ dispersion (after CF at 3,000 rpm for 30 min) versus different organic dispersants. (D) XRD patterns of bulk $TaTe_2$ and 2D $TaTe_2$. (E and F) (E) Ta 4f and (F) Te 3d XPS spectra of 2D $TaTe_2$. (G–I) (G) Raman spectra, (H) EPR curves, and (I) N_2-TPD profiles of bulk $TaTe_2$ and 2D $TaTe_2$ exfoliated in γ-BL.

relative intensity of the (001) was observed, suggesting loss of orientation in the plane as a consequence of exfoliation. The diffraction peak at 27.7° can be matched with tantalum oxide (JCPDS no. 19-1299), indicating partial oxidation under ultrasound liquid exfoliation. X-ray photoelectron spectroscopy (XPS) was employed to probe the surface chemical state of $TaTe_2$ nanosheets (Figure 1E); the main peaks centered at 25.8 and 27.7 eV correspond to Ta $4f_{7/2}$ and Ta $4f_{5/2}$, respectively, denoting a main valence state of Ta^{4+}.[29,30] The weak peaks appearing at 22.9 and 24.8 eV arise from TaO_x defects. Two doublet peaks can be seen with Te $3d_{5/2}$ at 572.8 and 576.1 eV and Te $3d_{3/2}$ at 583.2 and 586.5 eV attributed to respective Te^{2-} and Te^0 (Figure 1F).[31,32] Although metallic Te and TaO_x were also present in bulk $TaTe_2$ (arising from the Te precursor remaining during CVD synthesis of $TaTe_2$ and its surface oxidation upon exposure to air) (Figure S5), the fractions of Te^0 increased after exfoliation, suggesting the formation of Te vacancies in $TaTe_2$ nanosheets. Whereas the ratio of TaO_x/Ta^{4+} noticeably decreased after the exfoliation. An apparent O 1s XPS peak at 532.0 eV originating from adsorbed oxygen species was discernible (Figure S6). Figure 1G shows representative Raman spectra of bulk $TaTe_2$ and $TaTe_2$ nanosheets, with two prominent resonance peaks at around 122 and 141 cm^{-1} being associated with the in-plane E_g vibration mode and the out-of-plane A_{1g} vibration mode, respectively.[33] The effective restoring forces acting on the atoms increase concomitantly with layer number due to the interlayer van der Waals interaction, leading to a blue shift of the out-of-plane A_{1g} vibration. This tendency indicates that $TaTe_2$ nanosheets become increasingly ultrathin. Further electron paramagnetic resonance (EPR) spectroscopy was employed to detect paramagnetic signals, allowing for analysis of the unsaturated sites with unpaired electrons in catalyst (Figure 1H). Bulk $TaTe_2$ displayed weak EPR signals, suggesting low level of defects. By contrast, exfoliated $TaTe_2$ showed a symmetric pair of sharp peaks with the signal at g = 2.003, arising from trapped unpaired electrons by Te

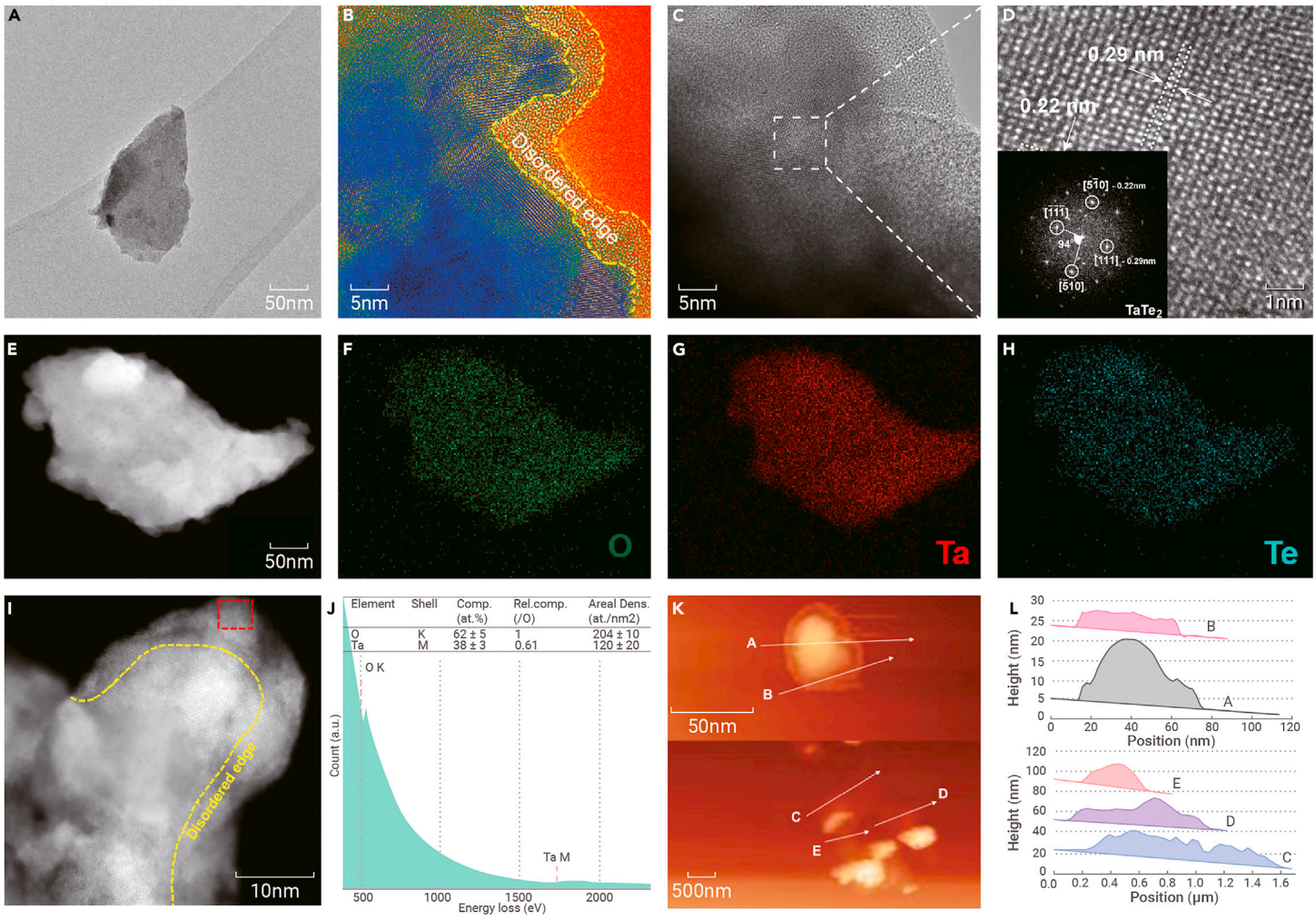

Figure 2. Morphology and Structure Characterization of 2D $TaTe_2$ (A) Low-magnification TEM image of 2D $TaTe_2$. (B) Transformed TEM image of Figure S8A. (C and D) HRTEM images of 2D $TaTe_2$, the inset in (D) is the corresponding fast Fourier transform pattern. (E–H) (E) HAADF-STEM image of $TaTe_2$ nanosheets and elemental maps of (F) O, (G) Ta, and (H) Te. (I and J) (I) HAADF-STEM image of $TaTe_2$ nanosheets and (J) corresponding electron energy loss spectroscopy spectrum, showing Ta and O edges. (K) Tapping-mode atomic force microscopy image of 2D $TaTe_2$ in γ-BL at a concentration of 0.4 mg mL^{-1} deposited on an SiO_2/Si substrate. (L) Corresponding line sections of image (K).

vacancies through adsorbed oxygen species from air (O^{2-}), in accord with XPS results.

Bulk $TaTe_2$ and $TaTe_2$ nanosheets exhibited type II N_2 adsorption/desorption isotherms in the Brunauer-Deming-Deming-Teller classification (Figure S7). After exfoliation, the Brunauer-Emmett-Teller surface area and average single-point total pore volume rose from <2.0 $m^2\ g^{-1}$ to 0.0112 $cm^3\ g^{-1}$ to 59.8 $m^2\ g^{-1}$ and 0.160 $cm^3\ g^{-1}$, respectively. The substantial increase in specific surface area benefits mass transport and improves surface accessibility to reactants, thus favoring NRR. We performed N_2 temperature-programmed desorption (N_2 TPD) to investigate the N_2 adsorption ability of $TaTe_2$. The N_2 TPD profiles of $TaTe_2$ nanosheets show two strong peaks at 338.6 °C and 411.0 °C, and a mild peak at 97.4 °C, arising from chemisorption and physisorption of N_2, respectively (Figure 1I). In comparison, only weak signals of physi- and chemisorbed N_2 on bulk $TaTe_2$ were detected, implying that $TaTe_2$ nanosheets possess more exposed active sites. The activation energy of desorption from the surface of $TaTe_2$ nanosheets was estimated to be about 32.6 kJ mol^{-1}, an indication of strong adsorption.[34] The superior N_2 adsorption capacity and high bonding-affinity toward N_2 of 2D $TaTe_2$ definitely provide benefits for electrocatalytic N_2 reduction.

Transmission electron microscopy (TEM) images showed the formation of thin $TaTe_2$ flakes with lateral sizes in the range of 200 nm to 1 μm, randomly stacking on top of each other (Figures 2A–2C and S8). Figure 2D reveals a set of interference fringes, with the fast Fourier transform showing *d*-spacings of 0.29 and 0.22 nm, and a mutual angle between the planes of 94°. These are in excellent agreement to 1T $TaTe_2$ viewed down the [15-6] axis, and with the 0.29 nm spacing corresponding to a {111} plane.[35] The existing oxygen means that $TaTe_2$ flakes were weakly oxidized on the surface, with disordered edges observed for many of the nanosheets (Figures 2B, 2I, and S8A).

High-angle annular dark-field scanning transmission electron microscopy (HAADF-STEM) observation (Figure 2E) together with *in situ* energy-dispersive X-ray spectroscopy mapping (Figures 2F–2H) indicated that $TaTe_2$ nanosheets were composed of Ta, Te, and a small amount of oxygen. Ta M and O K could only be detected in the electron energy loss spectroscopy spectrum (Figure 2J), and the Ta/O atomic ratio was about 0.61, corresponding to TaO_x in the XRD pattern. Shown in Figure 2K are the tapping-mode atomic force microscopy images of $TaTe_2$ dispersions deposited on an SiO_2/Si substrate. Flakes with measured heights of about 5, 13, 18, and 21 nm were observed. The average thickness of $TaTe_2$ exfoliated in γ-BL at a concentration of 0.1 mg mL^{-1} was estimated to be 4.5 nm (Figure S9).

Electrocatalytic property for N_2 reduction

To limit water availability close to the catalyst surface, the hydrophilic electrode surface was modified by TMHFS. It is expected that diminishing proton concentrations at the electrochemical interface by such hydrophobic modification can mitigate competition with the HER and thus boost the NRR. This can be explained by two aspects. On the one hand, the rate of hydrogen production was modeled to be the first order in the electron and proton concentrations, while the rate of NH_3 production was zeroth order in both. On the other hand, it is unlikely for electrochemical reduction of N_2 to be kinetically limited by proton concentration in electrolyte.[3] Figure 3A shows the contact angles of $TaTe_2$ nanosheets before and after hydrophobic treatment. Pristine $TaTe_2$ nanosheets is hydrophilic with

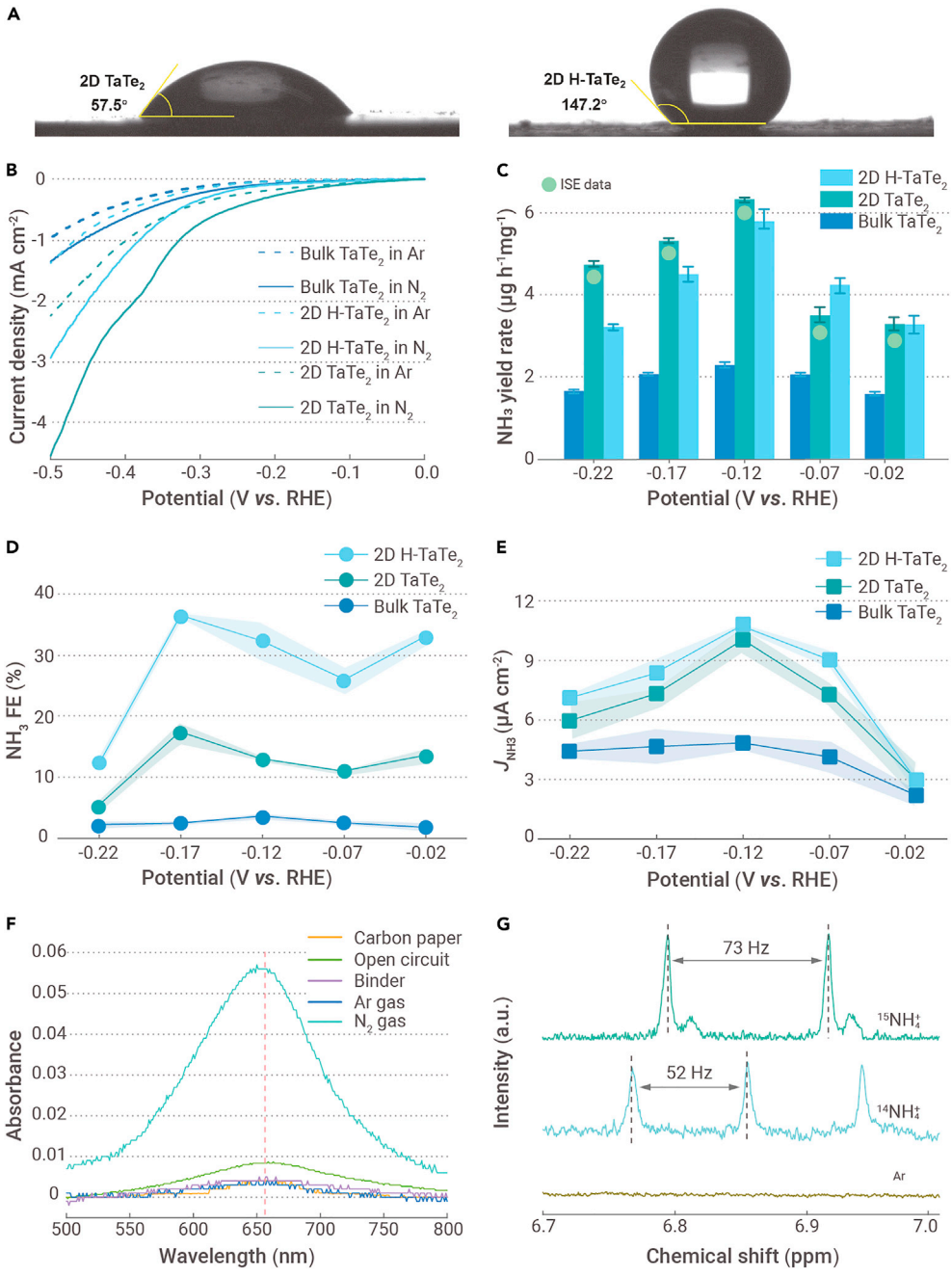

Figure 3. Contact Angle Results and Electrochemical Nitrogen Reduction Activities (A) The water contact angles of 2D $TaTe_2$ and H-$TaTe_2$. (B) The linear sweep voltammetry curves of bulk $TaTe_2$, 2D $TaTe_2$, and H-$TaTe_2$ in Ar-purged (dashed line) or N_2-purged (solid line) 0.1 M HCl solutions with a scan rate of 5 mV s^{-1}. (C and D) (C) The yield rates and (D) FEs of NH_3 over 2D H-$TaTe_2$, $TaTe_2$ nanosheets, and bulk $TaTe_2$. The NH_3 yield rates obtained by ion selective electrode are also included, as indicated by the green balls (ISE data). Data are represented as mean ± SE. (E) NH_3 partial geometric current densities over 2D H-$TaTe_2$, $TaTe_2$ nanosheets, and bulk $TaTe_2$ at different potentials. Data are represented as mean ± SE. (F) UV-vis absorption spectra of the electrolyte after electrolysis at −0.12 V in either Ar-saturated electrolyte (Ar gas), or without catalyst (Carbon paper), or with the binder (Binder), or at an open circuit potential (Open circuit, i.e., I = 0). (G) ^{1}H NMR spectra for the electrolyte after electrolysis at −0.12 V in $^{14}N_2$, $^{15}N_2$, and Ar-saturated 0.1 M HCl over 2D $TaTe_2$.

a contact angle of 57.5°. In stark contrast, after hydrophobic treatment, the hydrophilic electrode showed an increased contact angle of 147.2°, indicating a hydrophobic feature of 2D H-$TaTe_2$. The $TaTe_2$ nanosheets before and after the hydrophobic modification were examined for NRR using a classic two-compartment H-type cell separated by a cation-exchange membrane (Nafion 117) with continuous N_2 bubbling (Figure S10).

Particular care was taken when carrying out NRR to avoid false positives from background NH_3 in the system or external contamination. Prior to NRR measurements, the N_2 feeding gas was pre-purified to eliminate possible NH_3 and labile nitrogen-containing contaminants (such as nitric oxides, nitrates, or nitrites).[36] Spectrophotometric tests verified that almost no NO_3^- and NO_2^- existed in the N_2-purged electrolyte (Figures S11–S13). To evaluate the NRR activity, electrochemical tests were conducted in 0.1 M HCl solutions saturated with purified N_2 or Ar (Figure S14) was used as a feed gas. Linear sweep voltammetry curves of bulk $TaTe_2$, 2D $TaTe_2$, and H-$TaTe_2$ revealed an onset cathodic current related to hydrogen evolution under both Ar and N_2 conditions (Figure 3B). The 2D H-$TaTe_2$ exhibited a lower current density compared with 2D $TaTe_2$ in 0.1 M N_2-purged HCl, resulting from weak binding of hydrogen atoms on the hydrophobic surface. The NRR was found to take place with an overpotential as low as 294 mV (given the equilibrium thermodynamic potential for N_2 reduction to NH_4^+ is 0.274 V versus normal hydrogen electrode under 298 K and 1 atm) over $TaTe_2$ (Figure 3C).[3] Under the reaction conditions adopted, only NH_4^+ ions were detected by the indophenol blue method.[36] No N_2H_4 as by-product was identified by the Watt and Chrisp method within the detection limit of the method. Also, no NO_2^- and NO_3^- were detectable, excluding the occurrence of oxidation of nitrogen to NO_x by OH.[37] There are marginal NH_4^+ adsorbed by the Nafion 117 membrane in the H-type cell (Figures S15 and S16). The NH_3 formation rate over the catalysts increased within the switching potential range from −0.02 to −0.12 V, but dropped when further elevating the overpotential probably due to limitation in desorption and transport of formed NH_4^+ out of the catalyst surface (Figures 3C and S17). $TaTe_2$ nanosheets attained an averaged NH_3 yield rate of 6.3 μg_{NH3} h^{-1} mg_{cat}^{-1} with an FE of 12.9% at −0.12 V, nearly three times higher than that of bulk $TaTe_2$ and also significantly surpassing Te, TeO_2, Ta_2O_5, and corresponding hybrids with 2D $TaTe_2$ (Figure S18). The total current density increased with overpotential approaching 0.71 mA mg^{-1} at −0.22 V (Figure S19). The conversions of N_2 fed to NH_3 were estimated to be approximately 3.8 × 10^{-4}% at −0.12 V, considerably higher than that of a recently reported liquid H_2O droplet plasma system.[37] The NH_3 FE first decreased from −0.02 to −0.07 V because the HER tended to dominate over NRR at low overpotentials, but increased with applied potentials upon stepping the voltage from −0.07 to −0.17 V, beyond which the FE for NH_3 formation drastically declined owing to more severe competition from the HER. This may be linked to the possibility that high reaction rates increased the local pH value, consequently favoring alkaline water reduction, which could shift the reaction selectivity toward the HER. Moreover, at high current densities the available amounts of N_2 may become mass transport determined and decreased as a result of NRR. Among others, the wetted surface area within the electrode itself and occupation of active sites by *H (decreasing the surface coverage of $*N_2$) increased as a function of the applied reductive potential, which would also intensify the HER. The NH_3 FE attained was up to ~17.3% at −0.17 V, over seven times higher than that of bulk $TaTe_2$. Notably, H-$TaTe_2$ nanosheets reached an NH_3 FE exceeding 32.0% with an NH_3 formation rate of 5.8 μg_{NH3} h^{-1} mg_{cat}^{-1} at −0.12 V. The NH_3 FE could be further improved to 36.2% at −0.17 V, over 15 times higher than that of bulk $TaTe_2$ (Figure 3D). The NH_3 partial geometric current density of 2D H-$TaTe_2$ was 10.8 μA cm^{-2}, 2.3 times higher than that of bulk $TaTe_2$ (Figure 3E). The cathodic energy efficiency at

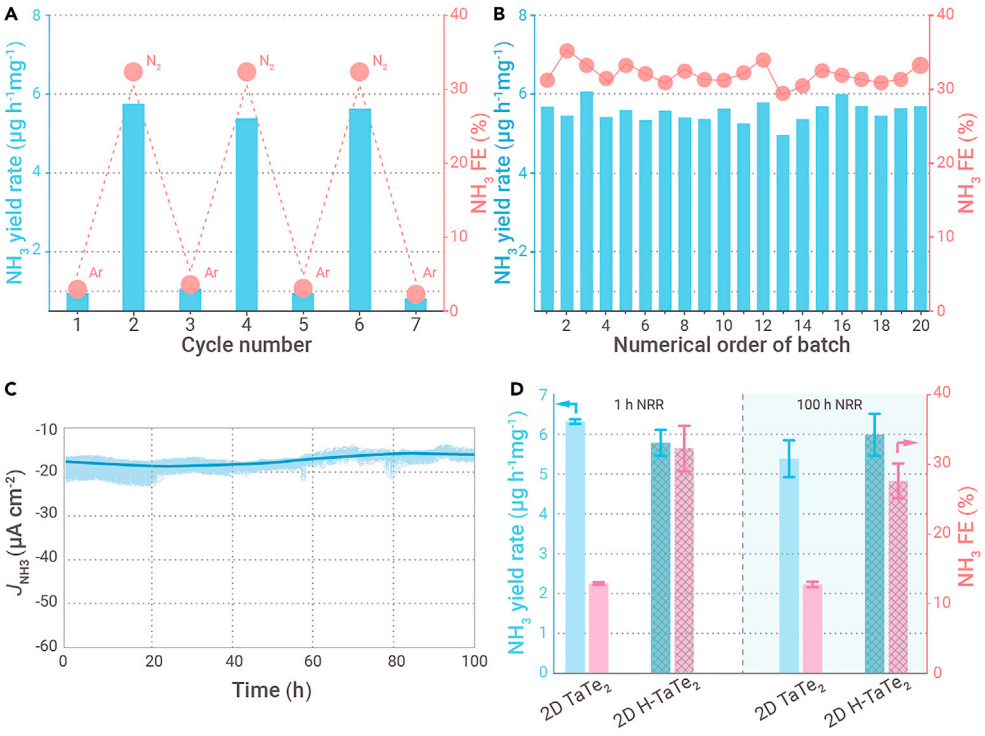

Figure 4. Stability Test Results (A) The NH_3 yield rate (bar) and FE (ball) with alternated Ar and N_2 cycles over 2D H-$TaTe_2$ at −0.12 V. (B) The NH_3 yield rates (bar) and FEs (ball) for 20 times by use of 20 batches of 2D H-$TaTe_2$ at −0.12 V. (C and D) (C) Long time stability and (D) NH_3 yield rates and FEs at −0.12 V over initial 2D H-$TaTe_2$ and $TaTe_2$ nanosheets after subjected to 100 h of operation. Data in (D) are represented as mean ± SE.

0.28 mA cm^{-2} was evaluated to be ~24.8% (Figure S20). The N_2 reduction performance was found to be most optimal at pH 1.0 (Figure S21) and a working electrode loading density of 0.5 mg_{TaTe2} cm^{-2} (Figure S22). Alternatively, both NH_3 production rate and FE were observed to increase with an increase of centrifugation speed from 500 to 1,000 rpm (Figure S23), indicating that increase in vacancy concentration led to improvement of NRR activity. Whereas further increase of centrifugation speed from 1,000 to 3,000 rpm to induce more defects (i.e., V_{Te}) resulted in decreased NRR performance. This may be due to lowering in electric conductivity and simultaneously enhanced HER. It is worth noting that the 2D H-$TaTe_2$ nanosheets outperform most previously reported transition metal- and precious metal-based electrocatalysts in terms of NH_3 FE (Table S2).[3]

To probe possible interference, if any, from the environment and assess the origin of the detected NH_3, a set of rigorous control and verification experiments (for multiple repeats at each condition) were carried out. Almost no NH_3 was obtained either in Ar-saturated solution (under the same conditions as the NRR experiments), or in the absence of catalyst, or with just the background Nafion solution binder, or at an open circuit potential (Figures 3F and 3G). Isotopic labeling using $^{15}N_2$ in combination with isotope-sensitive proton nuclear magnetic resonance (^{1}H NMR) was further performed. The ^{1}H NMR spectrum of the NRR product exhibited a doublet coupling (~73 Hz) typical for $^{15}NH_4^+$ compared with a triplet coupling (~52 Hz) for $^{14}NH_4^+$ (Figure 3G). The absolute dominant $^{15}NH_4^+$ doublets confirmed that the N in NH_3 stemmed from the gaseous N_2 supplied. In addition, we would like to emphasize that the $TaTe_2$ catalysts neither contain nitrogen in their structures nor are prepared from nitrates, nitrides, or ammonium precursors, excluding extraneous nitrogen sources. These strongly suggest that the NH_3 was generated from the reduction of dissolved N_2 accelerated by the 2D $TaTe_2$ electrocatalyst.

To evaluate the stability of 2D H-$TaTe_2$, we conducted alternating electrolysis between Ar and N_2-saturated electrolytes, which showed that the NH_3 evolved remained essentially unchanged for three cycles (Figure 4A). $TaTe_2$ nanosheets also exhibited good stability with nearly constant NH_3 yield rates, FEs, and partial geometric current densities (J_{NH3}) for 20 times by use of 20 batches of 2D

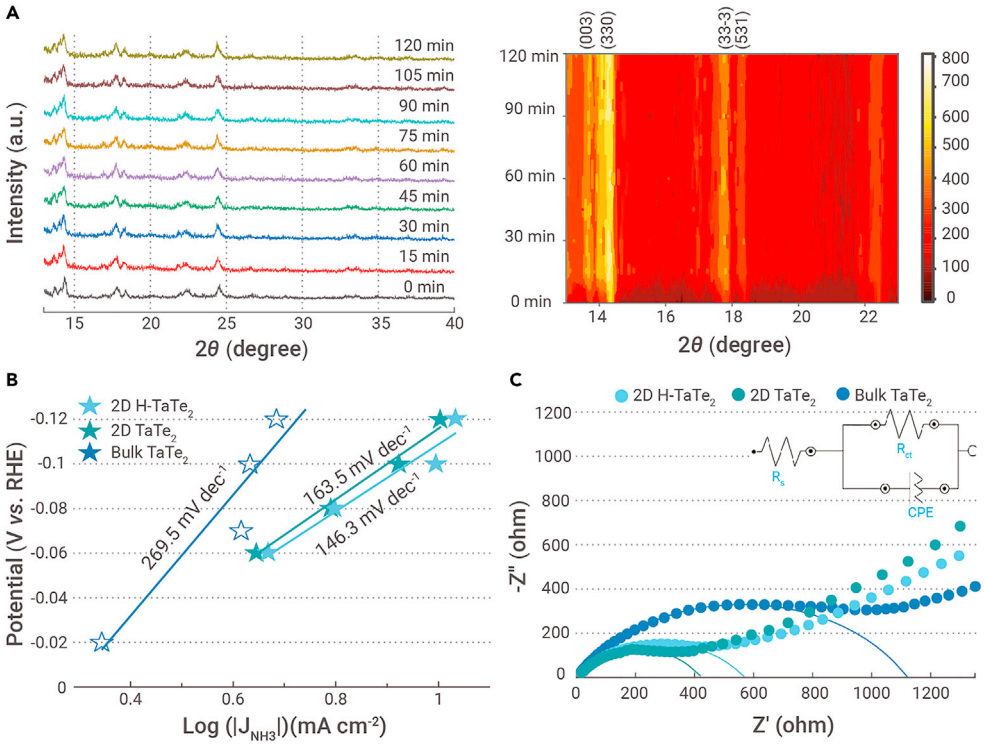

Figure 5. *In-situ* Measurements and Kinetics Analysis (A) *In situ* XRD profiles of 2D $TaTe_2$ at −0.12 V for 2 h of operation. (B and C) (B) Tafel plots and (C) Nyquist profiles of bulk $TaTe_2$, 2D $TaTe_2$, and H-$TaTe_2$.

H-$TaTe_2$ at −0.12 V (Figure 4B). Strikingly, negligible decay in J_{NH3} occurred even after continuous electrolysis for 100 h, indicating considerable catalytic stability of 2D H-$TaTe_2$ (Figure 4C). After 100 h of NRR, the catalytic performance of post-NRR 2D H-$TaTe_2$ and $TaTe_2$ in fresh N_2-saturated electrolyte was also determined. As displayed in Figure 4D, there are no obvious decreases in both NH_3 yield and FE at −0.12 V, suggesting that H-$TaTe_2$ nanosheets still maintained high activity after long-term use. No obvious leaching of $TaTe_2$ into the electrolyte (<0.06 wt %) was observed even after 100 h of electrolysis by inductively coupled plasma atomic emission spectroscopy analysis. The stability of $TaTe_2$ nanosheets was also investigated by *in situ* XRD analysis (Figures 5A and S24). It can be clearly seen that the peaks corresponding to $TaTe_2$ remained consistent throughout the entire electrolysis, accounting for the good durability of such V_{Te}-rich $TaTe_2$. Post characterization by

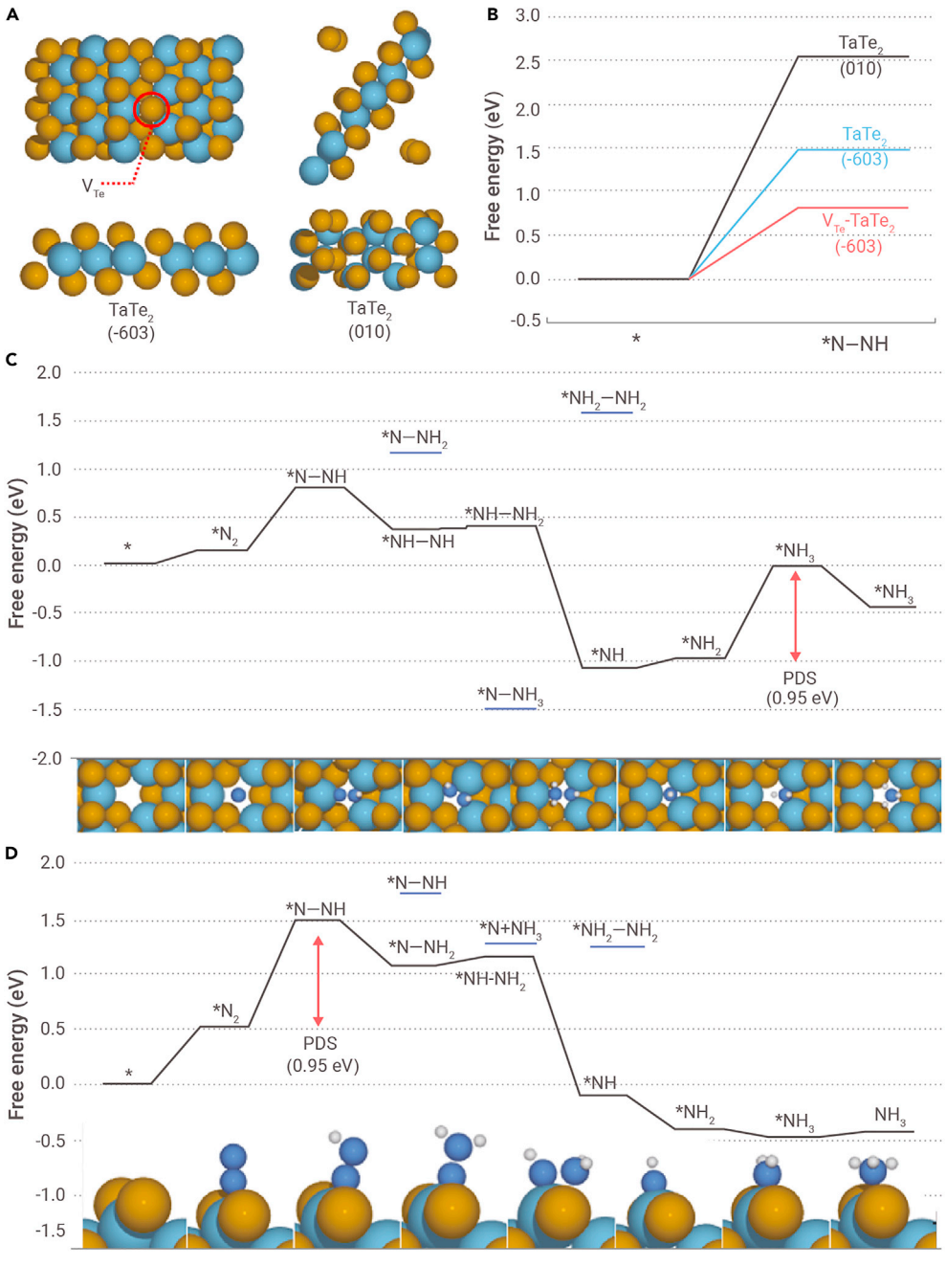

Figure 6. Calculation Models and Free Energy Diagrams for NRR (A) Top view (upper panel) and side view (lower panel) of the optimized structures of $TaTe_2$(−603) (left) and $TaTe_2$(010) (right). (B) The free energy change for *N–NH formation on $TaTe_2$(−603), V_{Te}-$TaTe_2$(−603), and $TaTe_2$(010). (C) The free energy diagram for NRR at 0 V (versus RHE) on V_{Te}-$TaTe_2$(−603). (D) The free energy diagram for NRR at 0 V (versus RHE) on $TaTe_2$(010). Free energies for less stable intermediate are represented by the blue line. Sky blue, yellow, blue, and white balls represent Ta, Te, N, and H atoms, respectively.

EPR (Figure S25) showed preservation of defects in 2D $TaTe_2$ even after electrolysis, accounting for maintenance of the NRR performance.

To gain insight into the outstanding activity of $TaTe_2$ nanosheets, the Tafel plot and electrochemical impedance were evaluated. The Tafel slope was ~146.3 mV dec^{-1} for 2D H-$TaTe_2$, ~163.5 mV dec^{-1} for $TaTe_2$ nanosheets, much lower than that of bulk $TaTe_2$ (~269.5 mV dec^{-1}) (Figure 5B). This implies that exfoliated $TaTe_2$ nanosheets possess more rapid reaction kinetics, and the first electron transfer process to yield *N–NH (* represents the surface adsorbed species) is the rate-determining step.[36] Nyquist plots (Figure 5C) revealed a significantly lower charge transfer resistance for H-$TaTe_2$ and $TaTe_2$ nanosheets than that for bulk $TaTe_2$, in accordance with its observed superior NRR activity.

To help understand the reaction mechanism for NRR and origin for enhanced NRR activity on $TaTe_2$ nanosheets, we conducted DFT calculations. We used monoclinic-$TaTe_2$, which agrees with the as-obtained crystalline structure of $TaTe_2$ from the XRD results (Figure 1D). The (−603) facet, which is the basal plane of the exfoliated $TaTe_2$, was considered. EPR characterization (Figure 1H) identified the emerging Te vacancy (V_{Te}) after exfoliation, and thus we also considered the NRR activity at V_{Te} sites. The V_{Te} site is modeled by eliminating one Te atom in $TaTe_2$(−603) (Figure S26), the most stable vacancy site is considered, denoted as V_{Te}-$TaTe_2$(−603). The TEM and STEM images (Figures 2B and 2I) showed the disordered edges. Making a representative DFT model for amorphous solid is limited due to the need for reasonable calculation times.[38] Alternatively, we used the crystalline edge of $TaTe_2$(010) instead, assuming that the local moiety of the amorphous edge to be similar to the crystalline edge. To investigate the effect of the TaO_x in the edge site, we modeled the oxygen atom containing $TaTe_2$(010) edge sites. Also, we constructed Te(10-10) facet to consider the remaining Te which were found in XPS (Figure 1F). The optimized geometries of calculation models are shown in Figures 6A and S27. We consider surface Ta atom as an active site in $TaTe_2$(010) and V_{Te}-$TaTe_2$(−603). For $TaTe_2$(−603), Te atom is regarded as an active site since Ta atom is not exposed.

Among the many intermediate steps in NRR, we first focused on *N–NH formation. This has been identified as the largest free energy demanding step in various catalysts and, hence, the *N–NH formation energy is a good descriptor for estimating the NRR activity.[39] We compared the *N–NH formation free energy on (−603), V_{Te}-$TaTe_2$(−603), and $TaTe_2$(010), obtained by G(*N–NH)−G(*)−G(N_2(g))−G(H^+ + e^-) (Figure 6B). The *N–NH formation free energy is noticeably decreased on $TaTe_2$(010) (1.47 eV) and V_{Te}-$TaTe_2$(−603) (0.82 eV) compared with that on $TaTe_2$(−603) (2.53 eV). We also found that N_2 does not chemically bind at Te atom in $TaTe_2$(−603) (Figure S28). This result indicates that the Ta atom site rather than Te atom facilitates *N–NH formation and plays an important role in enhancing N_2 activation. Meanwhile, the *N–NH formation energies of Te(10-10) (3.41 eV) and TaO_x (1.62–3.44 eV) are higher than that of V_{Te}-$TaTe_2$(−603) (0.82 eV) or $TaTe_2$(010) (1.47 eV) (Figure S27C). Thus, the Te and TaO_x are less reactive for NRR than V_{Te}-$TaTe_2$ and $TaTe_2$(010), which qualitatively agrees with the experimental result (Figure S18). We further conducted DFT calculations with the oxygen-doped $TaTe_2$(010), which showed the reliable *N–NH formation energy (1.66 eV, 1.63 eV) to consider the effect of the oxygen.

Next, we obtained a free energy diagram for NRR and identified the lowest free energy pathway. The NRR activity is estimated by comparing the free energy change at the potential-determining step (PDS), the largest free energy requiring electrochemical step. The PDS is *N_2 + (H^+ + e^-) → *N–NH on $TaTe_2$(−603) and $TaTe_2$(010) (Figures S28 and 6D), while that on V_{Te}-$TaTe_2$(−603) is *NH_2 + (H^+ + e^-) → *NH_3 (Figure 6C). We noted that a stronger N binding on V_{Te}-$TaTe_2$(−603) than $TaTe_2$(010) and $TaTe_2$(−603) leads to the different PDS. The theoretical volcano plot for NRR on transition metal surfaces showed a trend that the PDS of strong N binding metal and weak N binding metal is usually *NH_2 + (H^+ + e^-) → NH_3 and * + N_2 + (H^+ + e^-) → *N–NH, respectively.[39] Also, we found that *N–NH, the first electron transfer step, shows the highest apparent

energy in the free energy diagram of V_{Te}-$TaTe_2$(−603) and $TaTe_2$(010). This result matches the Tafel slope analysis, which reveals that the rate-determining step is the first electron transfer step.

As summarized in Figure S30, the free energy change at PDS increases in the order of $TaTe_2$(010) < V_{Te}-$TaTe_2$(−603) < $TaTe_2$(−603). Interestingly, the free energy change at PDS on $TaTe_2$(010) and V_{Te}-$TaTe_2$(−603) is decreased by ~1.8 eV compared with that of $TaTe_2$(−603), indicating that the exposed Ta atoms in $TaTe_2$, rather than surface Te atom, act as the major active sites for NRR. We note that the free energy change at PDS on $TaTe_2$(010) and V_{Te}-$TaTe_2$(−603) (0.95 eV) is comparable with the values (~1.0 eV) at the top of the NRR volcanoes on various transition metal surfaces.[39] In the case of oxygen-doped $TaTe_2$(010) planes, the PDS is $*N_2 + (H^+ + e^-) \rightarrow *N–NH$ and the free energy changes at the PDS are 0.96 and 0.93 eV (Figure S29), which are similar to that of $TaTe_2$(010) (0.95 eV). These results indicate that the presence of an amorphous TaO_x may not have a critical effect on catalytic activity.

CONCLUSIONS

In summary, we have demonstrated high yield of stably dispersed few-layer metallic $TaTe_2$ nanosheets rich in Te vacancies by ultrasonication of bulk $TaTe_2$ in γ-butyrolactone. The defective 2D $TaTe_2$ efficiently facilitated electrochemical N_2 fixation, delivering a large NH_3 FE (~12.9%) and high NH_3 formation rate (~6.3 $\mu g_{NH3}\ h^{-1}\ mg_{cat}^{-1}$) at an applied potential of −0.12 V. Facile modification of $TaTe_2$ electrodes by using trimethoxy (1H,1H,2H,2H heptadecafluorodecyl) silane substantially inhibited the parasitic HER and greatly increased the FE for NH_3 formation, reaching ~32.2% at −0.12 V with an NH_3 yield rate of 5.8 $\mu g_{NH3}\ h^{-1}\ mg_{cat}^{-1}$. The NH_3 FE was further improved to ~36.2% at −0.17 V, over 15.4 times higher than on bulk $TaTe_2$. Of particular interest is that the H-$TaTe_2$ nanosheets retained NRR performance even after 100 h of operation. DFT calculations showed that the exposed Ta atom sites dramatically enhanced N binding and decreased the free energy change at PDS, thereby boosting N_2 reduction. We envision that the integral strategy by engineering anion vacancies and surface hydrophobicity of 2D TMDs will offer profound implications for design and preparation of efficient NRR electrocatalysts.

REFERENCES

1. Andersen, S.Z., Čolić, V., Yang, S., et al. (2019). A rigorous electrochemical ammonia synthesis protocol with quantitative isotope measurements. Nature ***570***, 504–508.
2. Guo, J., and Chen, P. (2017). Catalyst: NH_3 as an energy carrier. Chem ***3***, 709–712.
3. Shen, H., Choi, C., Masa, J., et al. (2021). Electrochemical ammonia synthesis: mechanistic understanding and catalyst design. Chem ***7***, 1708–1754.
4. Wang, M., Houlton, B.Z., Wang, S., et al. (2021). Human-caused increase in reactive nitrogen burial in sediment of global lakes. The Innovation ***2***, 100158. https://doi.org/10.1016/j.xinn.2021.100158.
5. Zheng, J., Lyu, Y., Qiao, M., et al. (2019). Tuning the electron localization of gold enables the control of nitrogen-to-ammonia fixation. Angew. Chem. Int. Ed. ***58***, 18604–18609.
6. Li, Y., Li, X., Pillai, H.S., et al. (2020). Ternary PtIrNi catalysts for efficient electrochemical ammonia oxidation. ACS Catal. ***10***, 3945–3957.
7. Han, Z., Choi, C., Hong, S., et al. (2019). Activated TiO_2 with tuned vacancy for efficient electrochemical nitrogen reduction. Appl. Catal. B Environ. ***257***, 117896.
8. Zhao, Y., Shi, R., Bian, X., et al. (2019). Ammonia detection methods in photocatalytic and electrocatalytic experiments: how to improve the reliability of NH_3 production rates? Adv. Sci. ***6***, 1802109.
9. Shen, H., Peppel, T., Stunk, J., et al. (2020). Photocatalytic reduction of CO_2 by metal-free-based materials: recent advances and future perspective. Solar RRL ***4***, 1900546.
10. Chen, J.M. (2021). Carbon neutrality: toward a sustainable future. Innovation ***2***, 100127. https://doi.org/10.1016/j.xinn.2021.100127.
11. Chen, J.G., Crooks, R.M., Seefeldt, L.C., et al. (2018). Beyond fossil fuel-driven nitrogen transformations. Science ***360***, eaar6611.
12. Guo, C., Ran, J., Vasileff, A., et al. (2018). Rational design of electrocatalysts and photo(electro) catalysts for nitrogen reduction to ammonia (NH_3) under ambient conditions. Energy Environ. Sci. ***11***, 45–56.
13. Tao, H., Choi, C., Ding, L.-X., et al. (2019). Nitrogen fixation by Ru single-atom electrocatalytic reduction. Chem ***5***, 204–214.
14. Zhang, M., Choi, C., Huo, R., et al. (2020). Reduced graphene oxides with engineered defects enable efficient electrochemical reduction of dinitrogen to ammonia in wide pH range. Nano Energy ***68***, 104323.
15. Xu, T., Ma, D., Li, C., et al. (2020). Ambient electrochemical NH_3 synthesis from N_2 and water enabled by ZrO_2 nanoparticles. Chem. Commun. ***56***, 3673–3676.
16. Cheng, H., Ding, L.X., Chen, G.F., et al. (2018). Molybdenum carbide nanodots enable efficient electrocatalytic nitrogen fixation under ambient conditions. Adv. Mater. ***30***, 1803694.
17. Zhu, X., Wu, T., Ji, L., et al. (2020). Unusual electrochemical N_2 reduction activity in an earth-abundant iron catalyst via phosphorous modulation. Chem. Commun. ***56***, 731–734.
18. Cui, X., Tang, C., and Zhang, Q. (2018). A Review of electrocatalytic reduction of dinitrogen to ammonia under ambient conditions. Adv. Energy Mater. ***8***, 1800369.
19. Su, H., Chen, L., Chen, Y., et al. (2020). Single atoms of iron on MoS_2 nanosheets for N_2 electroreduction into ammonia. Angew. Chem. Int. Ed. ***59***, 20411–20416.
20. Yang, T., Song, T.T., Zhou, J., et al. (2020). High-throughput screening of transition metal single atom catalysts anchored on molybdenum disulfide for nitrogen fixation. Nano Energy ***68***, 104304.
21. Tao, H., Fan, Q., Ma, T., et al. (2020). Two-dimensional materials for energy conversion and storage. Prog. Mater. Sci. ***111***, 100637.
22. Zou, X., Xu, Y., and Duan, W. (2021). 2D materials: rising star for future applications. The Innovation ***2***, 100115. https://doi.org/10.1016/j.xinn.2021.100115.
23. Li, X., Li, T., Ma, Y., et al. (2018). Boosted electrocatalytic N_2 reduction to NH_3 by defect-rich MoS_2 nanoflower. Adv. Energy Mater. ***8***, 1801357.
24. Tao, H., Sun, X., Back, S., et al. (2018). Doping palladium with tellurium for the highly selective electrocatalytic reduction of aqueous CO_2 to CO. Chem. Sci. ***9***, 483–487.
25. Chen, X., Liu, Y.-T., Ma, C., et al. (2019). Self-organized growth of flower-like SnS_2 and forest-like ZnS nanoarrays on nickel foam for synergistic superiority in electrochemical ammonia synthesis. J. Mater. Chem. A ***7***, 22235–22241.
26. Chakravarty, D., Kumar, P., Ugale, V.S., et al. (2015). Microwave-assisted synthesis of few-layered $TaTe_2$ and its application as supercapacitor. Eur. J. Inorg. Chem. ***9***, 1598–1603.
27. Fan, Q., Choi, C., Yan, C., et al. (2019). High-yield production of few-layer boron nanosheets for efficient electrocatalytic N_2 reduction. Chem. Commun. ***55***, 4246–4249.
28. Tao, H., Zhang, Y., Gao, Y., et al. (2017). Scalable exfoliation and dispersion of two-dimensional materials—an update. Phys. Chem. Chem. Phys. ***19***, 921–960.
29. Yan, Z., Jiang, C., Pope, T.R., et al. (2013). Phonon and thermal properties of exfoliated $TaSe_2$ thin films. J. Appl. Phys. ***114***, 204301.
30. Li, D., Song, X., Hu, L., et al. (2016). Study on electrical defects level in single layer two-dimensional Ta_2O_5. Chin. Phys. B ***25***, 047304.
31. Chia, X., Ambrosi, A., Lazar, P., et al. (2016). Electrocatalysis of layered group 5 metallic transition metal dichalcogenides (MX_2, M = V, Nb, and Ta; X = S, Se, and Te). J. Mater. Chem. A ***4***, 14241–14253.
32. McGuire, G.E., Schweitzer, G.K., and Carlson, T.A. (1973). Core electron binding energies in some Group IIIA, VB, and VIB compounds. Inorg. Chem. ***12***, 2450–2453.
33. Li, J., Zhao, B., Chen, P., et al. (2018). Synthesis of ultrathin metallic MTe_2 (M = V, Nb, Ta) single-crystalline nanoplates. Adv. Mater. ***30***, 1801043.
34. Amenomiya, Y., and Cvetanovic, R.J. (1963). Application of flash-desorption method to catalyst studies. I. Ethylene-alumina system. J. Phys. Chem. ***67***, 144–147.
35. Brown, B.E. (1966). The crystal structures of $NbTe_2$ and $TaTe_2$. Acta Cryst. ***20***, 264–267.
36. Yang, L., Choi, C., Hong, S., et al. (2020). Single yttrium sites on carbon-coated TiO_2 for efficient electrocatalytic N_2 reduction. Chem. Commun. ***56***, 10910–10913.
37. Toth, J.R., Abuyazid, N.H., Lacks, D.J., et al. (2020). A plasma-water droplet reactor for process-intensified, continuous nitrogen fixation at atmospheric pressure. ACS Sustain. Chem. Eng. ***8***, 14845–14854.
38. Tielens, F., Gierada, M., Handzlik, et al. (2020). Characterization of amorphous silica based catalysts using DFT computational methods. Catal. Today ***354***, 3–18.
39. Montoya, J.H., Tsai, C., Vojvodic, A., et al. (2015). The challenge of electrochemical ammonia synthesis: a new perspective on the role of nitrogen scaling relations. ChemSusChem ***8***, 2180–2186.

ACKNOWLEDGMENTS

This work was supported by the National Natural Science Foundation of China (no. 21972010), Beijing Natural Science Foundation (no. 2192039), the State Key Laboratory of Organic–Inorganic Composites (no. oic–201901001), Beijing University of Chemical Technology (XK180301), and NRF Korea (NRF-2016M3D1A1021147). A.W.R. thanks the facilities of the DCCEM, at the Materials Department, Oxford (EP/R010145/1).

AUTHOR CONTRIBUTIONS

Z.S. supervised the project. Z.S. and Z.Z. conceived the idea. Z.Z., X.H., and Z.L. conducted synthesis and electrochemical experiments. S.H. and A.W.R. carried out the electron microscopy. H.Z. and T.W.B.L. measured *in situ* XRD. J.P., C.C., and Y.J. performed DFT analysis. Z.S., Z.Z., J.P., and Y.J. wrote the manuscript and A.W.R. polished the language.

DECLARATION OF INTERESTS

The authors declare no competing interests.

SUPPLEMENTAL INFORMATION

Supplemental information can be found online at https://doi.org/10.1016/j.xinn.2021.100190.

LEAD CONTACT WEBSITE

http://nanocarbon.cn/